Supporting Information

MicroRNA Detection through DNAzyme-Mediated Disintegration of Magnetic Nanoparticle Assemblies

Bo Tian,[a,b,*] Yuanyuan Han,[a] Erik Wetterskog,[a] Marco Donolato,[c] Mikkel Fougt Hansen,[b] Peter Svedlindh,[a] and Mattias Strömberg[a,*]

[a] Department of Engineering Sciences, Uppsala University, The Ångström Laboratory, Box 534, SE-751 21 Uppsala, Sweden

[b] Department of Micro- and Nanotechnology, Technical University of Denmark, DTU Nanotech, Building 345B, DK-2800 Kongens Lyngby, Denmark

[c] BluSense Diagnostics, Fruebjergvej 3, DK-2100 Copenhagen, Denmark

Table of Contents

S1. Optomagnetic system description and optomagnetic measurement principle.

As illustrated in **Figure S1**, the set-up employed for optomagnetic effect measurement was based on an unfocused 405 nm laser source (Sony optical unit, Sony, JP) and a photodetector (PDA36A, Thorlabs Inc., U.S.A.). Powered by a software controlled current source, the laser source provided a linearly polarized light beam (diameter of 2 mm), and the polarization direction was oriented along the axis of the applied magnetic field. A disposable UV-transparent cuvette (REF 67.758.001, SARSTEDT, Nümbrecht, Germany) was positioned in the beam path, centred between a pair of electromagnets (1433428C, Murata Power Solutions Inc., U.S.A.). The optical path through the liquid in the cuvette was 10 mm. The distance between the electromagnets was 20 mm, and the distance between laser source and detector was 115 mm. The LabVIEW controlled electromagnets were powered by an AC source. The AC magnetic field was applied perpendicular to the laser beam, and the maximum AC magnetic field amplitude was limited to approximately 2.6 mT in the current set-up. The self-inductance of the electromagnets was corrected for to ensure constant field amplitude and phase at all frequencies. The laser, electromagnets, cuvette, and detector were covered during measurements to avoid interference from external light sources. The detector signal was converted from analogue to digital by a data acquisition unit (DAQ unit, NI USB-6341, National Instruments, U.S.A.), followed by further processing in the computer by a FFT enabled lock-in function.

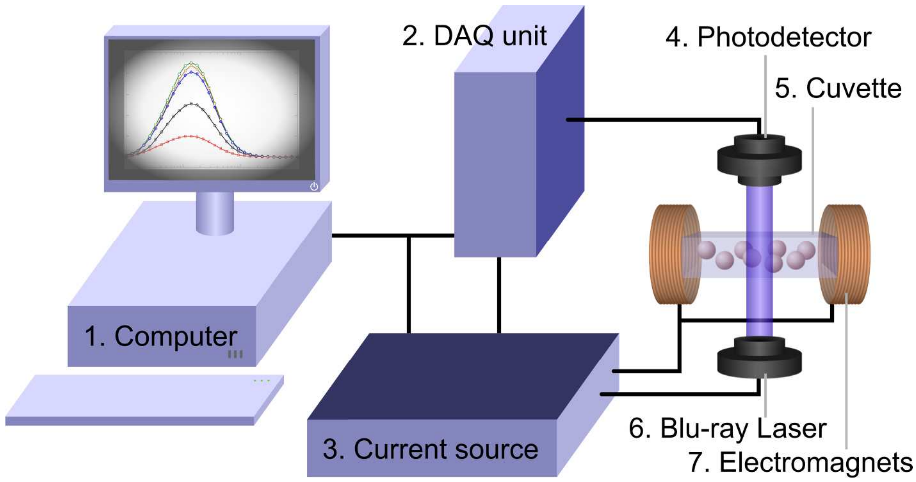

Figure S1. Schematic illustration of the optomagnetic set-up. The liquid sample, contained in an optically transparent cuvette (5), is placed between two identical electromagnets (7). A 405 nm laser source (6) generates a laser beam aimed at the bottom of the cuvette. The transmitted light detected by a photo detector (4) is recorded vs time using a DAQ unit (2). The laser and electromagnets are powered by a current source (3). A computer (1) controls the entire set-up and performs the software based lock-in detection.

The optomagnetic measurement principle is based on the rotational dynamics of magnetic nanoparticles (MNPs). The MNPs employed in this study have a remanent magnetic moment, which implies that the dominating relaxation mechanism upon a reversal of the magnetic field direction is a physical rotation of the particle, known as Brownian relaxation. The characteristic frequency for Brownian relaxation dynamics is given by

$$f_B = \frac{k_B T}{6\pi\eta V_h}, \tag{1}$$

where $k_B T$ is the thermal energy, η is the dynamic viscosity and V_h is the hydrodynamic volume of the relaxing entity (*e.g.*, a single MNP). The dynamic magnetic behavior can be described in term of the magnetic susceptibility χ with real (in-phase) and imaginary (out-of-phase) parts χ' and χ'', respectively. In case of a sinusoidal magnetic field $h_0 \sin(\omega t)$, the time dependent linear magnetic response can be expressed as

$$\chi(t) = M(t)/h_0 = \chi_0 \sin(\omega t - \theta) = \chi' \sin(\omega t) + \chi'' \cos(\omega t), \tag{2}$$

where $\chi' = \chi_0 \cos(\theta)$ and $\chi'' = \chi_0 \sin(\theta)$. At low frequencies the MNPs are able to rotate and follow the magnetic field, and the response is in-phase with the applied field. Therefore χ' is maximal. The rotation of the MNPs starts to lag behind the applied field at higher frequencies, which leads to a decrease in the in-phase component χ' and a corresponding increase in the out-of-phase component χ''. The out-of-phase component χ'' attains its maximum value at the Brownian relaxation frequency f_B.

A simple approach to account for a distribution of MNP sizes was introduced by Cole and Cole (Cole, K. S.; Cole, R. H. Dispersion and Absorption in Dielectrics I. Alternating Current Characteristics. *J. Chem. Phys.* **1941,** *9*, 341-351) according to the following expression for the complex magnetic susceptibility

$$\chi(\omega) - \chi_\infty = \frac{\chi_0 - \chi_\infty}{1 + (i\omega\tau_B)^{1-\alpha}}, \tag{3}$$

where α is the Cole-Cole parameter (ranging from 0 to 1, a measure of the nanoparticle size distribution width), $\tau_B = (f_B)^{-1}$ is the Brownian relaxation time, $\omega = 2\pi f$ is the angular frequency of the applied field and χ_0 and χ_∞ are the zero and high frequency limits of χ.

The dynamics is determined by the rotational behavior of the individual MNPs, which follows the Brownian relaxation dynamics. The modulation of the transmitted light is found in the complex second harmonic voltage output from the photodetector

$$V_2 = V_2' + \mathrm{i}V_2'', \tag{4}$$

where V_2' and V_2'' are the in-phase and out-of-phase signals, respectively. The modulation is measured using a lock-in amplifier with the AC magnetic field excitation as reference. From the perspective of transmitted light, the MNP ensemble will scatter light equally for a positive and negative magnetic field of the same amplitude. We therefore assume that the photodetector signal can be described as

$$V(t) = V_0 + V_{AC}\left|\sin(\omega t - \theta)\right| = V_0 + c\chi_0\left|\sin(\omega t - \theta)\right|, \tag{5}$$

where V_0 represents the un-modulated part of the transmitted light (used here for normalization), $V_{AC} = c\chi_0$ is the amplitude of the frequency dependent signal and c is a constant. The photodetector signal can further be expressed using the Fourier series for $\left|\sin(\omega t - \theta)\right|$, yielding

$$V(t) = V_0 + c\chi_0\left[\frac{2}{\pi} - \frac{4}{\pi}\left(\frac{1}{3}\cos(2\omega t - 2\theta) + \frac{1}{15}\cos(4\omega t - 4\theta) + \ldots\right)\right]. \tag{6}$$

Specifically, the second harmonic signal is given by

$$\begin{aligned} V_2(t) &= -\frac{4c\chi_0}{3\pi}\cos(2\omega t - 2\theta) \\ &= -\frac{4c\chi_0}{3\pi}\left(\cos(2\omega t)\cos(2\theta) + \sin(2\omega t)\sin(2\theta)\right) \\ &= -\frac{4c\chi_0}{3\pi}\left(\cos(2\omega t)\left(\cos^2(\theta) - \sin^2(\theta)\right) + 2\sin(2\omega t)\sin(\theta)\cos(\theta)\right) \\ &= -\frac{4c\chi_0}{3\pi}\left(\cos(2\omega t)\left((\tilde{\chi}')^2 - (\tilde{\chi}'')^2\right) + 2\sin(2\omega t)\tilde{\chi}''\tilde{\chi}'\right) \end{aligned} \tag{7}$$

,

where $\tilde{\chi}' = \chi'/\chi_0$ and $\tilde{\chi}'' = \chi''/\chi_0$. The lock-in detected in-phase and out-of-phase components of the second harmonic signal therefore become (rms values)

$$\begin{aligned} V_2' &= -2V_2(0)\tilde{\chi}''\tilde{\chi}' \\ V_2'' &= -V_2(0)\left((\tilde{\chi}')^2 - (\tilde{\chi}'')^2\right) \end{aligned} \tag{8}$$

where $V_2(0) = 4c\chi_0/3\sqrt{2}\pi$ is the zero frequency limit of V_2 (and V_2'').

The sign of V_{AC} depends on the optical scattering properties and the measurement geometry. For a geometry where the transmission is measured perpendicular to the axis of the applied magnetic field, as used in the present study, it is generally found that V_{AC} is negative for MNPs with sizes smaller than about 130 nm for blue laser light (λ = 405 nm). For even larger scattering entities, V_{AC} first becomes positive (*e.g.*, for 250 nm MNPs) and then negative (*e.g.*, for 500 nm MNPs). This originates from the oscillation of the scattering cross-section with particle size as can be accounted for by Mie scattering theory.

In **Figure S2a**, the normalized in-phase and out-of-phase components of the magnetic susceptibility, extracted from the Cole-Cole model, are plotted versus frequency. In **Figure S2b**, normalized $\tilde{\chi}'\tilde{\chi}''$ and $(\tilde{\chi}')^2 - (\tilde{\chi}'')^2$, have been plotted versus frequency to illustrate the shape of the two photodetector signals. The input susceptibilities, $\tilde{\chi}'$ and $\tilde{\chi}''$, are those displayed in **Figure S2a**.

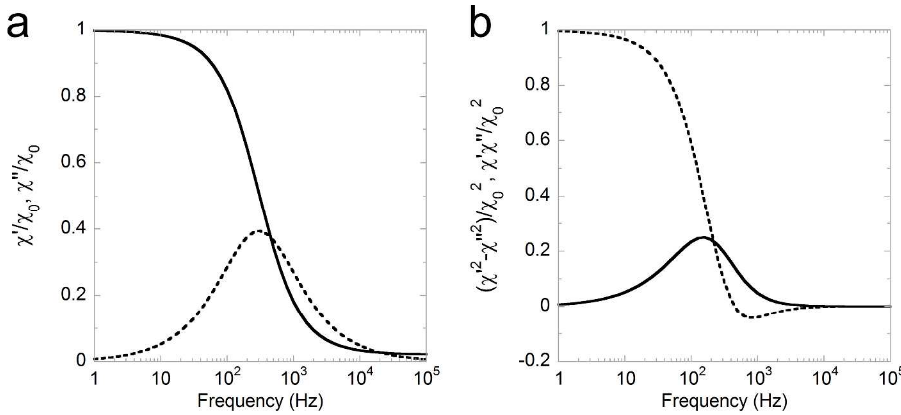

Figure S2. (a) Normalized susceptibility data (in-phase and out-of-phase represented by solid and dashed lines, respectively) extracted from the Cole-Cole model vs frequency (τ_B=300 s and α =0.15 were used as input). (b) Normalized $\tilde{\chi}'\tilde{\chi}''$ (solid line) and $(\tilde{\chi}')^2 - (\tilde{\chi}'')^2$ (dashed line) vs frequency. The $\tilde{\chi}'\tilde{\chi}''$ curve represents the in-phase signal from the photodetector, whereas the $(\tilde{\chi}')^2 - (\tilde{\chi}'')^2$ curve represents the out-of-phase signal from the photodetector.

S2. Evaluation of MNP assemblies employing different DNA:MNP ratios.

Low DNA loads on the particles may lead to small and loose assemblies; while high DNA loads means that more DNAzyme-based reactions are needed to release one single MNP, *i.e.*, low biosensing sensitivity. To achieve the best biosensing performance, we evaluated different MNP assemblies (DNA:MNP ratios of 5:1, 10:1, 20:1, 40:1 and 120:1) and tested their optomagnetic responses to 100 pM of target DNA. As shown in Figure S3, MNP assemblies employing DNA:MNP ratios of 20:1, 40:1 and 120:1 provide similar optomagnetic performances that are better than these based on DNA:MNP ratios of 5:1 and 10:1. To minimize the number of DNAzyme-based reactions needed for releasing one single MNP, we chose a DNA:MNP ratio of 20:1 for the proposed biosensing design.

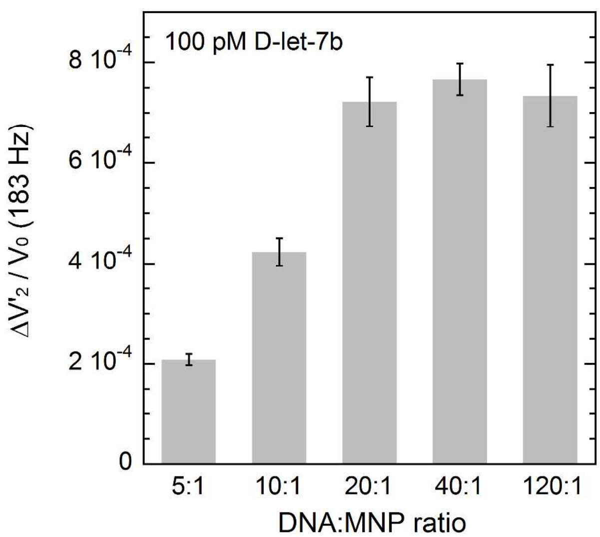

Figure S3. Optomagnetic signals of MNP assemblies based on different DNA loads. Different MNP assemblies using DNA:MNP ratios of 5:1, 10:1, 20:1, 40:1 and 120:1 were evaluated. MNA assemblies were incubated with 100 pM of D-let-7b and 5 nM of DZa at 50°C for 1 h. Error bars indicate the standard deviation based on three independent measurements.

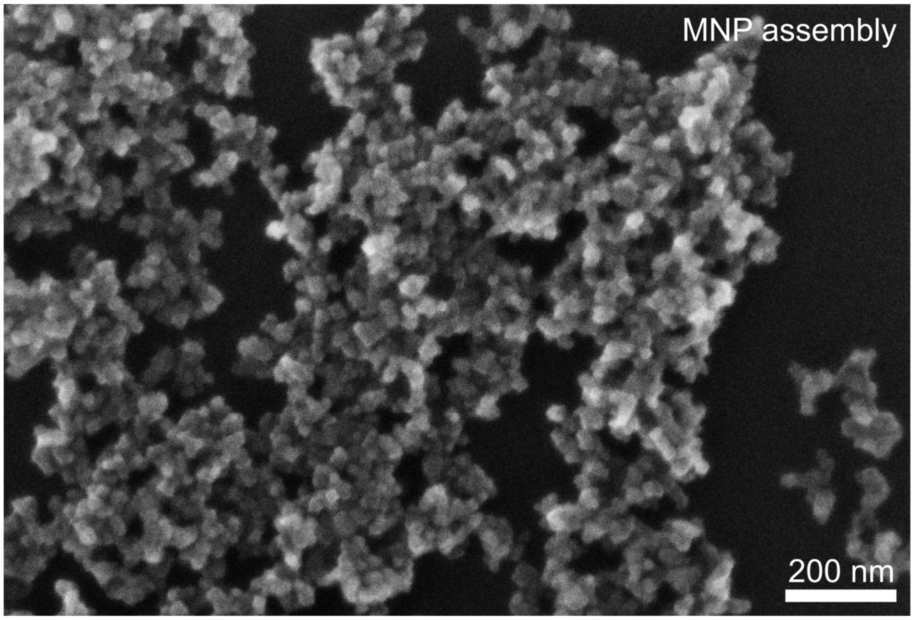

Figure S4. Observation of details of MNP assemblies using SEM. The arrangement of 100 nm MNPs cannot be resolved because each 100 nm MNP is a cluster of small single domain particles.

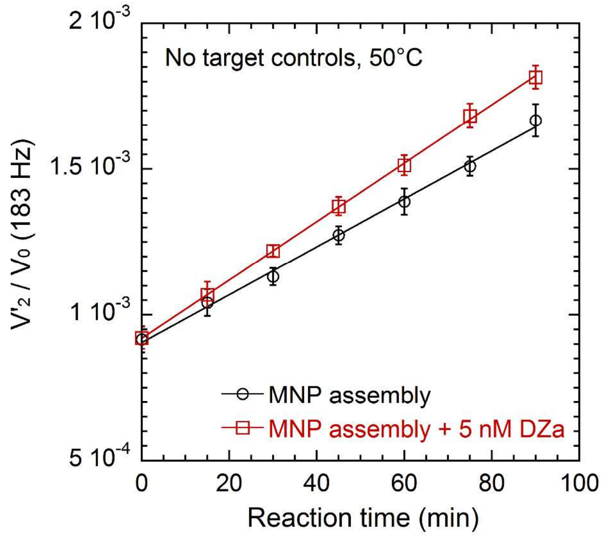

Figure S5. Time-resolved nonspecific disintegration of MNP assemblies. MNP assemblies were incubated at 50°C, with or without 5 nM of DZa. Time-resolved optomagnetic peak amplitudes were recorded, showing the nonspecific disintegration of MNP assemblies. Error bars indicate the standard deviation based on three independent measurements.

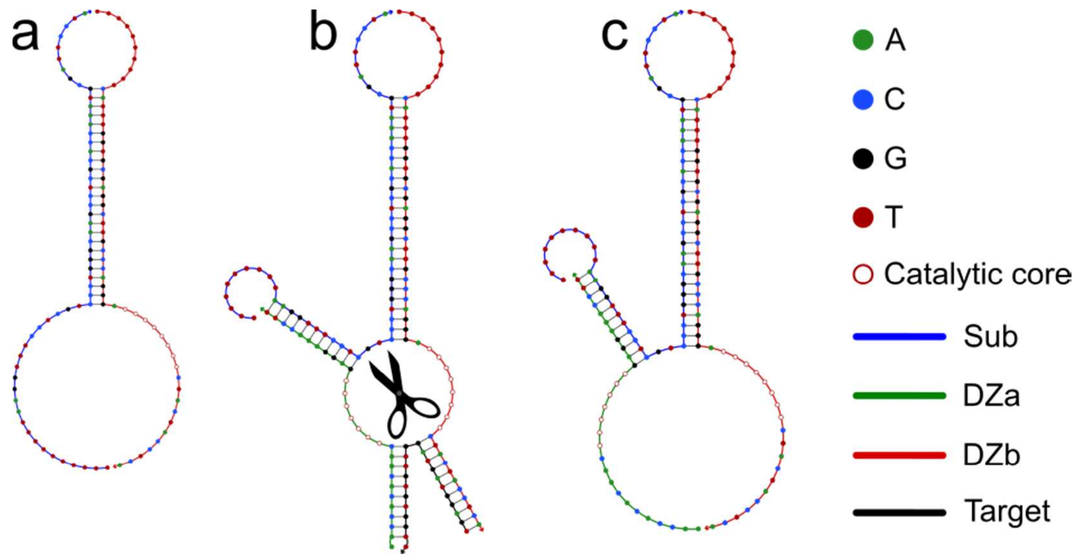

Figure S6. MFE secondary structures of (a) DNA scaffold, (b) MNAzyme, and (c) DZa-substrate-DZb at 50°C, analyzed by NUPACK. Sequences of catalytic core are replaced by poly T to avoid secondary structures formed in the catalytic core.